THE JOURNAL OF PHYSICAL CHEMISTRY B

pubs.acs.org/JPCB Article

Distinctive Morphology Modifiers for Polymer Blends: Roles of Asymmetric Janus Nanoparticles during Phase Separation

Qing Li, Liquan Wang,* Jiaping Lin,* and Zhanwen Xu

Cite This: J. Phys. Chem. B 2020, 124, 4619–4630 Read Online

ACCESS | Metrics & More | Article Recommendations | Supporting Information

ABSTRACT: Janus nanoparticles (JPs), which are anisotropic nanoparticles with multiple constituting parts, have been recognized as superior compatibilizers for polymer-blend-based nanocomposites. However, so far, most studies focused on the effects of symmetric JPs on the phase separation dynamics of polymer blends, while the roles of asymmetric JPs during phase separation remain unclear. In this work, the phase separation dynamics of symmetric blends compatibilized by JPs with various compositions was studied by using dissipative particle dynamics (DPD) simulations. It was found that the blends compatibilized by asymmetric JPs tend to undergo morphological transitions from bicontinuous networks to droplets-in-matrix structures at the late stage of phase separation, which is due to the influence of asymmetric JPs on the energetically favored curvature of the interfaces between polymer domains. Such a mechanism is absent for symmetric JPs and other compatibilizers (e.g., triblock copolymers and homogeneous particles) because they lack the unique combination of chemical asymmetry with the particulate nature like the asymmetric JPs. Moreover, it was observed that the asymmetric JPs can stably localize at the interfaces and act as efficient compatibilizers only when the fraction of the minor constituent part exceeds a critical value. These findings not only shed light upon the roles of asymmetric JPs as compatibilizers but also indicate a promising strategy for designing polymer-blend-based nanocomposites with tailor-made structures.

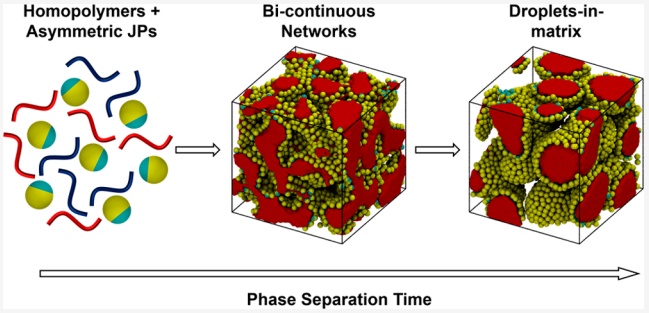

1. INTRODUCTION

Polymer blends, which are mixtures of at least two polymeric components,[1] have found applications in a lot of fields such as high-performance plastics,[2] organic photovoltaics,[3,4] battery electrolytes,[5,6] membranes,[7,8] supercapacitors,[9,10] automobile coatings,[11,12] adhesives,[13,14] etc. In many cases, the properties (e.g., mechanical,[2,15] dielectric,[16,17] and barrier[18] properties) of the blends are closely related with the morphologies of respective phases,[19] and compatibilizers like homogeneous nanoparticles and copolymers (block, graft, random, etc.) are usually incorporated to stabilize the blend morphologies during phase separation so that materials with controllable structures and optimized performance can be obtained.[20] Recently, Janus nanoparticles (JPs), which are anisotropic nanoparticles with at least two constituent parts,[21] have been recognized as superior compatibilizers in comparison to traditional ones because their unique combination of anisotropy with the Pickering effect endows them with a strong affinity to the polymer domain interfaces.[22−24] By this means, the drawbacks of traditional compatibilizers such as detachment from interfaces and formation of micelles can be effectively avoided.[25,26] Currently, JPs have been utilized to compatibilize not only model systems for scientific studies but also blend materials of technological relevance,[17,27,28] which demonstrates their versatility for practical purposes.

In addition to their interfacial activity, another important character of JPs is that the shapes and sizes of their constituent parts can be respectively changed,[29] which enables researchers to design and synthesize asymmetric JPs with diverse structures by a manifold of symmetry-breaking strategies such as self-assembly of block copolymers,[30] phase separation/inversion in confined space,[31] microfluidics,[32] and anisotropic growth of chemically different species.[33] Currently, such asymmetric JPs have received considerable interest from scholars working on multifunctional nanoplatforms,[34−36] and their applications regarding the compatibilization of polymer blends are also attracting increasing attention. Thus far, most of the existing studies in this field have been concerned with the snowman-like JPs with two unequally sized lobes,[37−40] which not only help to reduce the interfacial tension between polymer domains like symmetric JPs but also uniquely influence the morphologies of polymer blends.[40] For example,

Received: March 11, 2020
Revised: May 4, 2020
Published: May 7, 2020

https://dx.doi.org/10.1021/acs.jpcb.0c02165
J. Phys. Chem. B 2020, 124, 4619–4630

You et al. studied the morphologies of poly(lactic acid)/polycarbonate (PLA/PC) blends compatibilized by the asymmetric snowman-like JPs with a smaller SiO_2 lobe and a larger polystyrene (PS) lobe after the mixing and extrusion processes.[40] The PS lobe can selectively localize in the PC phase, which facilitates PC to form continuous networks even at low weight fractions. By this means, PLA/PC blends showing the bicontinuous morphologies can be easily prepared.

From the experiment work stated above, we learned that the composition of asymmetric JPs critically affects the connectivity of the dispersed phase in the JP-compatibilized blends, which implies a promising tool for the preparation of polymer blends with tailor-made morphologies. However, there is a large space of parameters (e.g., interactions between the structural units of polymers, volume fractions of respective components, and the composition of compatibilizers) for controlling the morphologies of compatibilized blends. Therefore, it may take a vast amount of experimental efforts to elucidate the effects of various parameters systematically.[41−44] In addition, elaboration of the underlying mechanisms is limited by the difficulties in characterization, which hinders the optimization of the structures of asymmetric JP-based compatibilizers. In comparison to experiments, theoretical simulations provide a useful tool for systematically illuminating the mechanisms governing the phase behavior of polymer blends.[45,46] Currently, a series of simulation methods have been adopted to study the phase separation dynamics of polymer blends, such as molecular dynamics (MD),[47] Monte Carlo (MC),[48] single-chain-in-mean-field (SCMF) theory,[49] and numerical methods based on the *H*-model.[50] Among these methods, dissipative particle dynamics (DPD), a coarse-graining method based on molecular dynamics (MD),[51] has attracted increasing attention because it offers much larger time and length scales in comparison to traditional MD-based methods.[52−55] For example, Yong et al. combined DPD simulations with machine learning to explore the phase behavior of bicomponent hydrogels compatibilized by JPs.[54] Morphology transitions from homogeneous mixtures to phase-separated structures as the radius of JPs increases or the concentration of JPs decreases were identified. Guo et al. used DPD simulations to investigate the influence of Janus nanospheres on the domain growth of polymer blends at the late stage of phase separation. They found that the domain growth at the late stage obeys an exponential law, and the growth rate drops with time due to the reduction of interfacial tension.[52,56] However, most of those reports focused on symmetric JPs, while much less attention has been paid to the mechanisms governing the behavior of asymmetric JPs as compatibilizers. Understanding such mechanisms can be of critical importance for the design and preparation of novel materials. To this point, DPD simulations may offer a useful tool to exploit the influence of asymmetric JPs on the morphology evolution of polymer blends during phase separation, as well as to elucidate the underlying mechanisms.

In this work, the phase separation dynamics of the polymer blends compatibilized by asymmetric JPs was studied by using DPD simulations. Specifically, we used the symmetric blends with equal amounts of unlike polymers as an example to illustrate the morphology evolution of blends during phase separation. The influence of asymmetric JPs with various compositions on the morphology evolution was observed, and the underlying mechanisms were analyzed based on the interfacial energy of JPs. Moreover, the compatibilization efficiency of asymmetric JPs was characterized. It was found that the asymmetric JPs uniquely induce the symmetric blends to undergo morphology transitions from bicontinuous networks to island structures at the late stage of phase separation, which is in remarkable contrast to other compatibilizers such as homogeneous nanoparticles and block copolymers. Lastly, the results presented in this work were compared with the experimental observations in the literature.

2. MODELS AND METHODS

2.1. DPD Method. In this work, the compatibilization behavior of asymmetric JPs was studied by using DPD simulations. This method has been widely adopted to study the phase separation dynamics of polymer blends because it is especially suitable for investigating the phase behavior of complex fluids.[52,54,55,57,58] In this method, each bead represents a lump of atomic (or molecular) matters, which interacts with one another via a soft repulsion vanishing at the cutoff distance r_c.[51] The interaction strength between the ith and jth beads is proportional to the interaction parameter a_{ij}, which is larger than 25 if the two beads are of unlike species and is equal to 25 if they are of identical or compatible species (see Table 1).[55] Reduced units are adopted in the DPD method, which means that the units of distance, mass, energy, and time are given by r_c, m, k_BT, and τ, respectively, where m is the mass of each bead, k_B is the Boltzmann constant, T is the temperature, and τ is the time unit given by $\tau = (mr_c^2/k_BT)^{1/2}$. More details of the DPD method are available in section 1 of the Supporting Information.

Table 1. Interaction Parameters a_{ij} between Different Components

a_{ij}	A	B	C
A	25	30−75	30−75
B		25	30−75
C			25

2.2. Models. The blending system studied in this work is based on the experiments of Bryson et al., who studied the morphologies of polystyrene/poly(methyl methacrylate) (PS/PMMA) blends compatibilized by symmetric JPs.[59] The JPs in their work consist of a polybutadiene (PB) core (3−5 nm) with several PS and PMMA chains emanating from it.[25,59] Figure 1 shows the coarse-grained models of the JPs adopted in this work. Each particle contains a spherical core of **C** with N_{J_A} **A** chains and N_{J_B} **B** chains. The beads of **A**, **B**, and **C** are denoted by J_A, J_B, and J_C, respectively. The core of the model

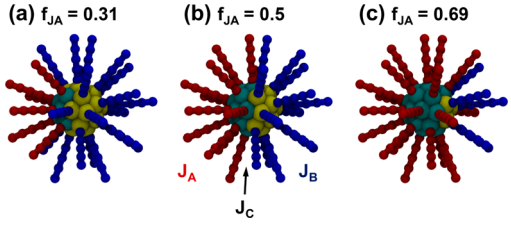

Figure 1. Coarse-grained models of asymmetric JPs with various compositions of (a) $f_{J_A} = 0.31$, (b) $f_{J_A} = 0.5$, and (c) $f_{J_A} = 0.69$. J_A and J_B beads are colored in red and blue, respectively. J_C beads connected with the J_A and J_B chains are colored in cyan and yellow, respectively.

https://dx.doi.org/10.1021/acs.jpcb.0c02165
J. Phys. Chem. B 2020, 124, 4619−4630

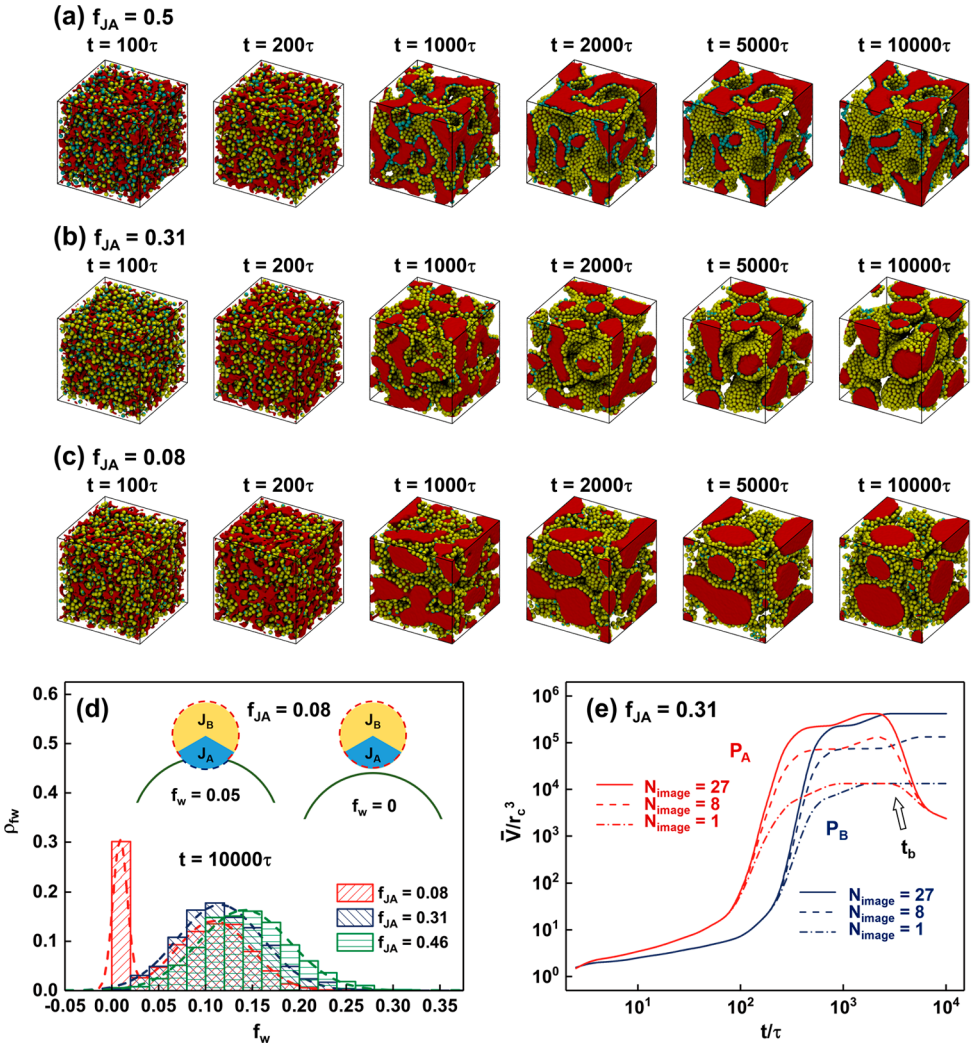

Figure 2. (a–c) Morphology evolution of P_A/P_B blends compatibilized by JPs with various compositions of (a) $f_{J_A} = 0.5$, (b) $f_{J_A} = 0.31$, and (c) $f_{J_A} = 0.08$. (d) Distribution ρ_{f_w} of the wrapping fraction f_w at $t = 10^4\tau$ for JPs with various f_{J_A}. Insets at the upper right corner show the physical meaning of f_w. (e) Log–log profiles of the average volume $\bar{V}(t)$ of the P_A and P_B domains calculated at various N_{image} values for the JPs with $f_{J_A} = 0.31$. The black arrow denotes the time t_b at which the network of P_A breaks into dispersed domains.

particle consists of 26 J_C beads that were uniformly packed into a sphere with radius $R_{core} = 1.55r_c$ and were restricted to move as a rigid body. Each J_C bead is grafted with a J_A block or a J_B block, which was modeled as a freely joining chain containing $N_{graft} = 5$ beads. Note that the JPs can be considered as *soft* nanoparticles because the J_A and J_B blocks are flexible chains and can change their chain conformations during the phase separation. The asymmetry of the particles was characterized *via* the composition f_{J_A}, which is given by

$$f_{J_A} = \frac{N_{J_A}}{N_{J_A} + N_{J_B}} \quad (1)$$

where N_{J_A} and N_{J_B} are the numbers of J_A and J_B chains, respectively. In this work, $N_{J_A} + N_{J_B}$ was fixed to be 26, and f_{J_A} was varied from 0.09 to 0.91. Two homopolymers of **A** and **B** were considered. They were modeled as freely joining chains of $N_{HP} = 50$ beads and were denoted by P_A and P_B, respectively. The radius of gyration, R_g, of the homopolymer chains is around $2.46r_c$. Note that, if we consider the R_{core} to be 5 nm, then the R_g of P_A and P_B is around 8 nm, which is comparable with the R_g (~9.5 nm) of PS in experiments.[25]

The interaction parameters between the species **A**, **B**, and **C** are listed in Table 1. The values of a_{ij} between unlike species were varied in the range 30–75 and are equal to 75 in this manuscript without special mentions. The volume fractions of JPs, P_A, and P_B are denoted by c_{JP}, c_{P_A}, and c_{P_B}, respectively, with the c_{JP} fixed to be 0.4, which is much higher than those in experiments because of the box size effect[56] (the average sizes of the P_A and P_B domains are comparable with the box size if c_{JP} is not sufficiently high). We focused on symmetric blends ($c_{P_A} = c_{P_B}$) because their phase separation dynamics in the absence of additives obeys the well-known spinodal decomposition (SD) mechanism,[60,61] which helps to identify the effects of JPs during the phase separation of polymer blends.

2.3. Simulation Procedures. We performed the simulations by using HOOMD-blue, which is a general-purpose particle simulation toolkit optimized for executions on both GPUs and CPUs.[62−64] All of the simulations in this work were performed in cubic boxes of size $L = 80r_c$, with the periodic

https://dx.doi.org/10.1021/acs.jpcb.0c02165
J. Phys. Chem. B 2020, 124, 4619−4630

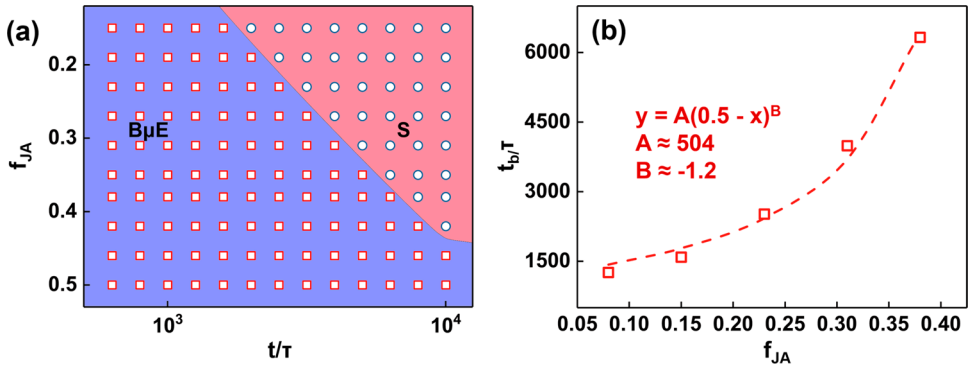

Figure 3. (a) Two-dimensional morphology diagram in the space of t and f_{J_A} indicating the regions of the bicontinuous network morphology (denoted by **BμE**) and the spheres-in-matrix morphology (denoted by **S**). (b) Dependence of the morphology transition time t_b on f_{J_A}. The dashed curve corresponds to the power law noted in the figure.

boundary condition (PBC) imposed on all of the three directions. The JPs and homopolymers were initially randomly placed in the box, with the a_{ij} between all species set to be 25. A preliminary simulation was performed for 5×10^4 time steps to thoroughly homogenize the system (the length of each time step is 0.02τ). The unfavorable interactions (Table 1) between unlike species were instantaneously turned on to trigger the phase separation process. The simulation then lasted for another 5×10^5 time steps until the equilibrium state was achieved.

3. RESULTS AND DISCUSSION

3.1. Morphology Evolution of Polymer Blends. We start with the phase separation dynamics of the polymer blends compatibilized by symmetric JPs. Figure 2a–c shows the morphology evolution during phase separation for the P_A/P_B blends compatibilized by JPs with various compositions. Here, the domains rich in P_A are colored in red, and the domains rich in P_B are not shown for clarity. The JPs are sketched as spheres with a J_A (cyan) surface region and a J_B (yellow) surface region. The morphologies of the blends become stable at late times ($t \geq 10^4\tau$; not shown here for brevity), indicating that the equilibrium states have been achieved. For the symmetric JPs with $f_{J_A} = 0.5$ (Figure 2a), after the start of phase separation, P_A and P_B gradually separate into bicontinuous networks ($t = 10^2$–$10^3\tau$), and the JPs are distributed at the P_A/P_B interfaces with the J_A and J_B surface regions oriented toward the P_A and P_B phases, respectively. At the late stage of phase separation ($t \geq 10^3\tau$), the size of the P_A/P_B domains grows with time, while the JPs remain exclusively located at the interfaces, which demonstrates that they can act as efficient compatibilizers. These observations agree well with the results in the literature,[25,52,55,65] suggesting that the method adopted here can reasonably reflect the phase behavior of JP-compatibilized blends.

The morphologies of the symmetric blends compatibilized by the asymmetric JPs with $f_{J_A} = 0.31$ and $f_{J_A} = 0.08$ are shown in Figure 2b and c, respectively. As shown in Figure 2b, the polymers P_A and P_B first form bicontinuous structures at the early stage of phase separation ($t \leq 10^3\tau$), which is similar to the systems compatibilized by symmetric JPs. However, we observed a transition from the bicontinuous network morphology to the *island* morphology during the late stage ($10^3\tau \leq t \leq 10^4\tau$), with P_A and P_B forming the droplet phase and the matrix phase, respectively. Note that such a morphology transition is beyond the predictions of traditional SD theories, which state that the two components of an SD system will spontaneously form bicontinuous networks if their volume fractions and viscosities are both identical. Therefore, a detailed elaboration of the mechanism underlying the morphology transition is highly valued.

Moreover, for the JPs with $f_{J_A} = 0.08$ (Figure 2c), we not only observed a morphology transition from the bicontinuous network structures to the droplets-in-matrix structures ($10^3\tau \leq t \leq 5 \times 10^3\tau$) analogous to the case of $f_{J_A} = 0.31$ (Figure 2b) but also found obvious detachment of the JPs from the interfaces at the late stage of phase separation, which indicates a reduction of the efficiency of JPs. In order to monitor the efficiency of the JPs with various compositions, we used the fraction f_w of the particle surface wrapped by the P_A domains to characterize the spatial distribution of JPs (see the insets of Figure 2d). Note that $f_w > 0$ suggests that the particle is located at the interface, while $f_w = 0$ suggests that it has been detached from the interface. Figure 2d shows the fraction ρ_{f_w} of the particles with corresponding f_w at $t = 10^4\tau$ for the JPs with $f_{J_A} = 0.46$, $f_{J_A} = 0.31$, and $f_{J_A} = 0.08$. For the JPs with $f_{J_A} = 0.08$, a remarkable ρ_{f_w} peak at $f_w \approx 0$ can be observed, which indicates the detachment of JPs from the interfaces. Such a peak at $f_w \approx 0$ is absent for those with $f_{J_A} = 0.31$ and 0.46, confirming that they can steadily distribute at the interfaces during the late stage of phase separation. These results corroborate that the JPs with $f_{J_A} = 0.31$ and $f_{J_A} = 0.46$ can act as efficient compatibilizers, while the efficiency of the JPs with $f_{J_A} = 0.08$ is much lower.

In order to clearly characterize the morphology transition stated above for the asymmetric JPs (e.g., those with $f_{J_A} = 0.31$), we calculated the average volume $\bar{V}_A$ ($\bar{V}_B$) of the P_A (P_B) domains at various times with the effect of the periodic boundary condition (PBC) taken into account. Here, $\bar{V}$ is given by

$$\bar{V} = \int V \rho_V \, dV \tag{2}$$

where ρ_V is the volume fraction of the domains with corresponding V. Note that, in this work, the PBC was imposed on all of the three directions (i.e., x, y, and z), which means that each system actually contains an infinite number of identical boxes called *images*.[66] Therefore, when calculating the

https://dx.doi.org/10.1021/acs.jpcb.0c02165
J. Phys. Chem. B 2020, 124, 4619–4630

values of $\overline{V}_A$ and $\overline{V}_B$ for each system, we first built up an *expanded* box containing N_{image} images and then counted the volume of each domain in the expanded box. As shown in Figure S1, $\overline{V}_A$ ($\overline{V}_B$) is independent of N_{image} if P_A (P_B) forms dispersed domains but increases with increasing N_{image} if P_A (P_B) forms continuous networks. This suggests that the relationship between $\overline{V}(t)$ and N_{image} can be used to identify the morphology of polymer domains at a certain time t. If $\overline{V}(t)$ is dependent on N_{image}, then it can be deduced that continuous networks are formed; if $\overline{V}(t)$ is independent of N_{image}, one can then assert that the polymer forms dispersed droplets.

Figure 2e shows the log−log profiles of $\overline{V}_A$ and $\overline{V}_B$ calculated at various N_{image} values for the JPs with $f_{J_A} = 0.31$. The values of $\overline{V}_A$ and $\overline{V}_B$ rapidly grow as the phase separation progresses from $t = 10^2\tau$ to $t = 10^3\tau$ and both increase as N_{image} increases at $t \approx 10^3\tau$, reflecting the formation of bicontinuous P_A and P_B networks during the phase separation process. After that, $\overline{V}_A$ rapidly drops as the phase separation proceeds and becomes independent of N_{image} at $t \approx 10^4\tau$, which indicates the break of the P_A networks into dispersed domains. Meanwhile, $\overline{V}_B$ still depends on N_{image}, which is consistent with the formation of the P_B matrix. The time (denoted by t_b) corresponding to the maximum decreasing rate of $\overline{V}_A$ is thus regarded as the boundary between the bicontinuous networks regime and the island morphology regime ($t_b \approx 4 \times 10^3\tau$ in this case).

Based on the above method for identifying morphology transition times, we further built a two-dimensional diagram in the space of f_{J_A} and t to indicate the influence of asymmetric JPs on the morphology evolution of polymer blends during the phase separation process (Figure 3a). Note that the **BμE** (bicontinuous micro-emulsion) region corresponds to the bicontinuous network morphology, while the **S** region corresponds to the spheres-in-matrix morphology. It can be viewed from Figure 3a that the boundary between these two regions shifts toward the earlier times as f_{J_A} decreases, and the morphology transition times t_b at different f_{J_A} lie at the identical straight line in Figure 3a, which implies that $\log(t_b)$ is linearly related with f_{J_A} (note that Figure 3a is plotted in the single-log style). Based on the above observation, we plotted in Figure 3b the profile of t_b vs f_{J_A} for asymmetric JPs with $f_{J_A} \leq 0.4$ and fit the t_b−f_{J_A} relationship with the following power law

$$t_b = A(0.5 - f_{J_A})^B \tag{3}$$

where A and B are two fitting parameters ($A \approx 501$ and $B \approx -1.2$ in this work). We expect that the above t_b−f_{J_A} relationship is of considerable technological relevance. For the polymer-blend-based nanocomposites compatibilized by asymmetric JPs, one can first identify the values of the fitting parameters A and B and then control the morphologies of the materials by intentionally terminating the phase separation process before or after the transition time *via* liquid−solid approaches like crystallization or chemical cross-linking.[67,68] By this means, materials with tailor-made structures (e.g., island structures or bicontinuous network structures) can be designed and prepared.

In order to check the versatility of the above method, we varied the interaction parameters (i.e., a_{AB}, a_{AC}, and a_{BC}) from 30 to 75 (note that we fixed $a_{AB} = a_{BC} = a_{AC}$) and examined the phase separation dynamics of the JP-compatibilized blends. Here, the value of the interaction parameter a is proportional to the magnitude of the repulsive interactions between two neighbor DPD beads; therefore, a higher (or lower) value of a_{AB} means stronger (or weaker) incompatibility between the components **A** and **B** (a_{BC} and a_{AC} similarly). Figure S2 shows the equilibrium morphologies at various a_{AB} values for the JPs with $f_{J_A} = 0.31$. It can be viewed that the JPs effectively compatibilize the systems when a_{AB} is as low as 30, indicating that the above morphology-controlling method not only applies to the polymers with strong unlike interactions (e.g., $a_{AB} = 75$) but also to the polymers whose unlike interactions are weaker (e.g., $a_{AB} = 30$).

3.2. Mechanisms Underlying the Morphology Transitions. In subsection 3.1, it is shown that the blends compatibilized by the symmetric JPs with $f_{J_A} = 0.5$ show bicontinuous morphologies at the late stage of phase separation. This agrees well with the theories of the SD mechanism, which state that the two immiscible components spontaneously form bicontinuous structures if their viscosities and volume fractions are both identical. However, the blends compatibilized by the asymmetric JPs with $f_{J_A} = 0.31$ and $f_{J_A} = 0.08$ exhibit morphology transitions from bicontinuous networks to spheres-in-matrix structures, which is beyond the SD mechanism. Therefore, an in-depth elaboration of the underlying mechanism is required.

We first clarify at which time the interfacial jamming occurs because this is the prerequisite of obtaining equilibrium morphologies.[40] Figure 4 shows the profiles of the normalized

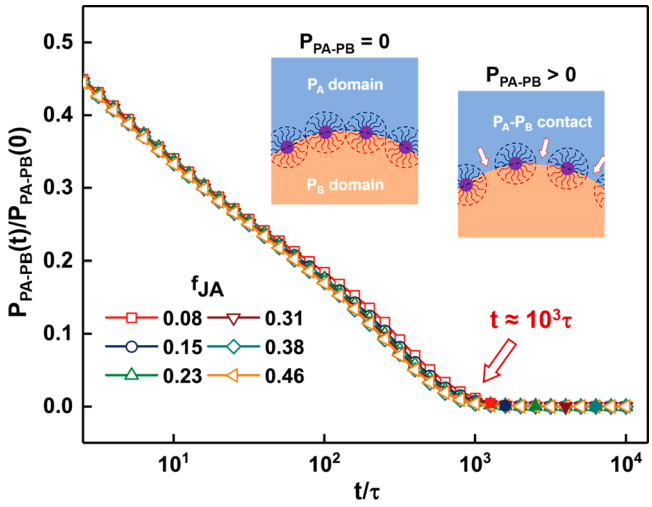

Figure 4. Normalized P_A−P_B contact probability $P_{P_A-P_B}(t)/P_{P_A-P_B}(0)$ for JPs with various f_{J_A}. Morphology transition times are indicated by filled symbols. The inset on the left side shows a P_A/P_B interface totally covered by JPs (interfacial jamming). The inset on the right side shows an interface where the P_A and P_B beads can interact with each other through the interstices (denoted by white arrows) between particles.

P_A−P_B contact probability $P_{P_A-P_B}(t)/P_{P_A-P_B}(0)$ for the JPs with various f_{J_A}. Note that $P_{P_A-P_B}(t)/P_{P_A-P_B}(0) = 0$ suggests that the interface is completely covered by the JPs (interfacial jamming), while $P_{P_A-P_B}(t)/P_{P_A-P_B}(0) > 0$ suggests that there are interstices between the particles (see the insets of Figure 4). As shown in Figure 4, $P_{P_A-P_B}(t)/P_{P_A-P_B}(0)$ steadily decreases and vanishes at $t \approx 10^3\tau$, which marks the occurrence

https://dx.doi.org/10.1021/acs.jpcb.0c02165
J. Phys. Chem. B 2020, 124, 4619−4630

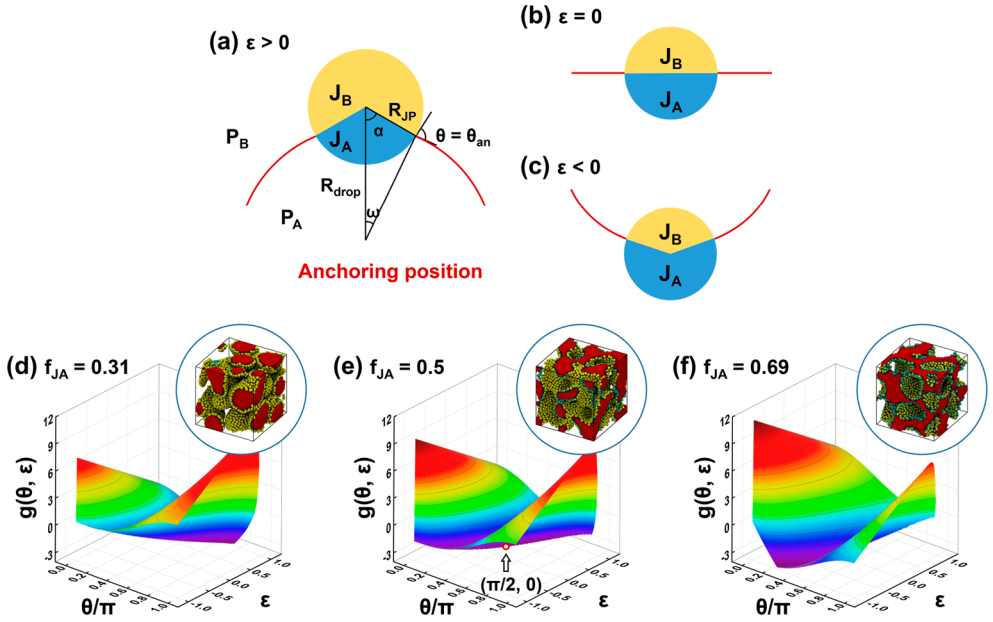

Figure 5. (a–c) Schematic illustration of three JPs with various compositions located at the P_A/P_B interfaces with various curvatures: (a) $f_{J_A} = 0.31$ and $\varepsilon > 0$, (b) $f_{J_A} = 0.5$ and $\varepsilon = 0$, and (c) $f_{J_A} = 0.69$ and $\varepsilon < 0$. J_A and J_B parts are colored in cyan and yellow, respectively. P_A/P_B interfaces are colored in red. (d–f) Dimensionless interfacial energy $g(\theta, \varepsilon)$ at $0 \le \theta \le 2\pi$ and $-1 \le \varepsilon \le 1$ for JPs with various compositions of (d) $f_{J_A} = 0.31$, (e) $f_{J_A} = 0.5$, and (f) $f_{J_A} = 0.69$. The graphs in the upper right corners show the blend morphologies at equilibrium. The black arrow in panel e indicates the minimum value of $g(\theta, \varepsilon)$.

of interfacial jamming. Note that the occurrence of interfacial jamming is before the morphology transitions (see Figure 3), suggesting that the unfavorable interactions between P_A and P_B do not play a determinant role in the morphology transitions.

Since the morphology transition follows the full coverage of the P_A/P_B interfaces by the JPs for all systems, we anticipate that the morphology transitions observed for asymmetric JPs may be driven by the interfacial energy of the JPs. According to Hirose et al., the adsorption energy E_{JP} of a JP with radius R_{JP} located at a droplet with radius R_{drop} is given by[69]

$$E_{JP} = 2\pi R_{JP}^2 \sigma_{P_AP_B}\left[g(\theta, \varepsilon) + \sigma + \sigma' \cos\alpha + \frac{R_{JP}(p_{P_A} + p_{P_B})}{3\sigma_{P_AP_B}}\right] \quad (4)$$

where σ_{mn} is the interfacial tension between the components m and n (m, n = P_A, P_B, J_A, J_B), $\sigma = (\sigma_{P_AJ_A} + \sigma_{P_BJ_B})/\sigma_{P_AJ_B}$ and $\sigma' = (\sigma_{P_AJ_A} - \sigma_{P_BJ_B})/\sigma_{P_AP_B}$ are two scaled interfacial tensions, p_{P_A} and p_{P_B} are the pressures of the P_A and P_B phases, respectively, θ is the contact angle measured across the P_A phase, α is the composition angle (see Figure 5a), ε is a dimensionless curvature given by

$$\varepsilon = \frac{R_{JP}}{R_{drop}} \quad (5)$$

[note that $\varepsilon = 0$ if the interface is flat (Figure 5b) and $\varepsilon > 0$ ($\varepsilon < 0$) if the interface is bent toward the P_A (P_B) phase (Figure 5a and c)], and $g(\theta, \varepsilon)$ is the dimensionless interfacial energy. Specifically, $g(\theta, \varepsilon)$ adopts the following form

$$g_A(\theta, \varepsilon) = \gamma_A[\cos(\theta - \omega) - \cos\alpha] - \frac{1 - \cos^3\omega}{3\varepsilon^2} - \frac{\varepsilon}{3}[3\cos(\theta - \omega) - \cos^3(\theta - \omega)] \quad (6)$$

for $\theta_{an} \le \theta \le \pi$ (case A), and

$$g_B(\theta, \varepsilon) = \gamma_B[\cos(\theta - \omega) - \cos\alpha] - \frac{1 - \cos^3\omega}{3\varepsilon^2} - \frac{\varepsilon}{3}[3\cos(\theta - \omega) - \cos^3(\theta - \omega)] \quad (7)$$

for $0 \le \theta \le \theta_{an}$ (case B), where $\gamma_A = (\sigma_{P_AJ_A} - \sigma_{P_BJ_A})/\sigma_{P_AP_B}$ and $\gamma_B = (\sigma_{P_AJ_B} - \sigma_{P_BJ_B})/\sigma_{P_AP_B}$ are two normalized interfacial tensions, ω is the central angle defined in Figure 5a, and θ_{an} is the contact angle corresponding to the anchoring position (i.e., the position at which the boundary between the J_A and J_B surface regions coincides with the P_A/P_B interface). (Details of $g(\theta, \varepsilon)$ are available in section 4 of the Supporting Information.) Parts d–f of Figure 5 show the values of $g(\theta, \varepsilon)$ at $0 \le \theta \le \pi$ and $-1 \le \varepsilon \le 1$ for the JPs with $f_{J_A} = 0.46$, $f_{J_A} = 0.5$, and $f_{J_A} = 0.69$, respectively. For the asymmetric JPs with $f_{J_A} = 0.46$ and $f_{J_A} = 0.69$, we found remarkable depressions in the $g(\theta, \varepsilon)$ profiles at the positive and negative ε regions, respectively, which suggests that the P_A-droplets-in-P_B-matrix and the P_B-droplets-in-P_A-matrix morphologies are energetically preferred for those JPs, respectively. In comparison, for the JPs with $f_{J_A} = 0.5$, we identified a minimum in $g(\theta, \varepsilon)$ at $\theta = \pi/2$ and $\varepsilon = 0$, indicating that the droplets-in-matrix morphology is unfavorable for them. These observations agree well with the equilibrium morphologies of the blends (see the graphs in the upper right corners of Figure 5d–f).

https://dx.doi.org/10.1021/acs.jpcb.0c02165
J. Phys. Chem. B 2020, 124, 4619–4630

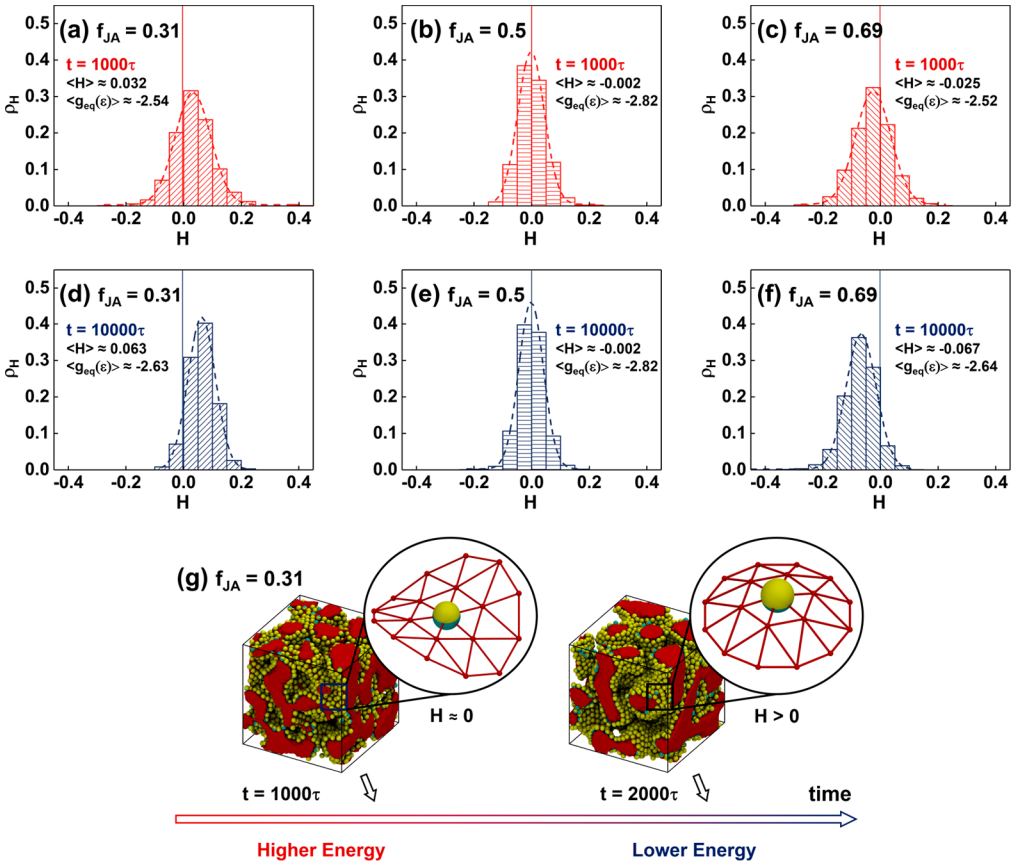

Figure 6. (a–f) Distribution ρ_H at $t = 10^3\tau$ (the upper row) and $t = 10^4\tau$ (the lower row) of the mean curvature H for P_A/P_B interfaces surrounding JPs with various compositions of (a, d) $f_{J_A} = 0.31$, (b, e) $f_{J_A} = 0.5$, and (c, f) $f_{J_A} = 0.69$. $H = 0$ is denoted by a vertical segment in each figure. Ensemble averages of the mean curvature H and the equilibrium interfacial energy $g_{eq}(\varepsilon)$ are denoted. (g) Schematic illustration of the mechanism underlying the breakage of the P_A networks for the JPs with $f_{J_A} = 0.31$. Graphs at the upper right corners schematically show the typical shapes of interfaces surrounding JPs.

Although the theory of Hirose et al. correctly predicts the equilibrium morphologies of the JP-compatibilized blends, it is difficult to use this theory to explain the morphology transitions during phase separation (Figure 2b,c) because it is difficult to get the values of R_{drop} and ε if both P_A and P_B form continuous networks. Therefore, we improved the theory of Hirose et al. by using the mean curvature H instead of ε when calculating the interfacial energies of the JPs during phase separation. Here, H is defined by

$$H = \frac{\kappa_1 + \kappa_2}{2} \tag{8}$$

where κ_1 and κ_2 are the two principal curvatures. H is formally related with ε by $\varepsilon = R_{JP}H$, which means that $H > 0$ ($H < 0$) if the interface is locally bent toward the J_A (J_B) surface region and $H = 0$ if the interface is locally flat (details of κ_1 and κ_2 are available in section 5 of the Supporting Information).

Parts a–f of Figure 6 show the distributions ρ_H of the mean curvature H for the P_A/P_B interfaces surrounding the JPs with various f_{J_A} at $t = 10^3\tau$ (Figure 6a–c) and $t = 10^4\tau$ (Figure 6d–f) (ρ_H is the fraction of the interfaces with corresponding H). For the JPs with $f_{J_A} = 0.31$, a large fraction of interfaces shows $H \approx 0$ (Figure 6a), which is consistent with the bicontinuous morphology at $t = 10^3\tau$ (see Figure 2e). The position of the ρ_H peak shifts toward the positive H region as the phase separation progresses from $t = 10^3\tau$ to $t = 10^4\tau$ (Figure 6d), and the value of $\langle H \rangle$ increases from 0.032 to 0.063, which correctly reflects the breakage of the P_A networks. Interestingly, such a shift in ρ_H actually leads to a decrease in $\langle g_{eq}(\varepsilon) \rangle$ from −2.54 to −2.63, corroborating that the P_A-droplets-in-P_B-matrix morphology is energetically more preferred than the bicontinuous network morphology (note that g_{eq} is the equilibrium interfacial energy; see eqs S14–S17 of the Supporting Information for details). Such a trend can also be observed for the JPs with $f_{J_A} = 0.69$ (compare Figure 6c with Figure 6f), as the dispersion of the P_B droplets in the P_A matrix (see Figure 5f) leads to a shift of the ρ_H peak position from $H \approx 0$ to the negative H region and simultaneously a decrease in $\langle g_{eq}(\varepsilon) \rangle$ from −2.52 to −2.64. Lastly, for the blends compatibilized by symmetric JPs, the ρ_H peak position remains at $H \approx 0$ and the value of $\langle H \rangle$ is stable (Figure 6b and e), confirming that the bicontinuous networks of P_A and P_B evolve steadily at the late stage of phase separation. Meanwhile, the value of $\langle g_{eq}(\varepsilon) \rangle$ keeps at a low level (~ -2.82), revealing that the bicontinuous network morphology is energetically favorable for the symmetric JPs.

The emerging physical picture based on the results shown in Figure 6a–f is as follows. For the JP-compatibilized blends, P_A and P_B initially phase separate *via* the SD mechanism and form bicontinuous structures at the early times of phase separation. For the symmetric JPs, such bicontinuous networks grow steadily at the late stages of phase separation, as they are

https://dx.doi.org/10.1021/acs.jpcb.0c02165
J. Phys. Chem. B 2020, 124, 4619–4630

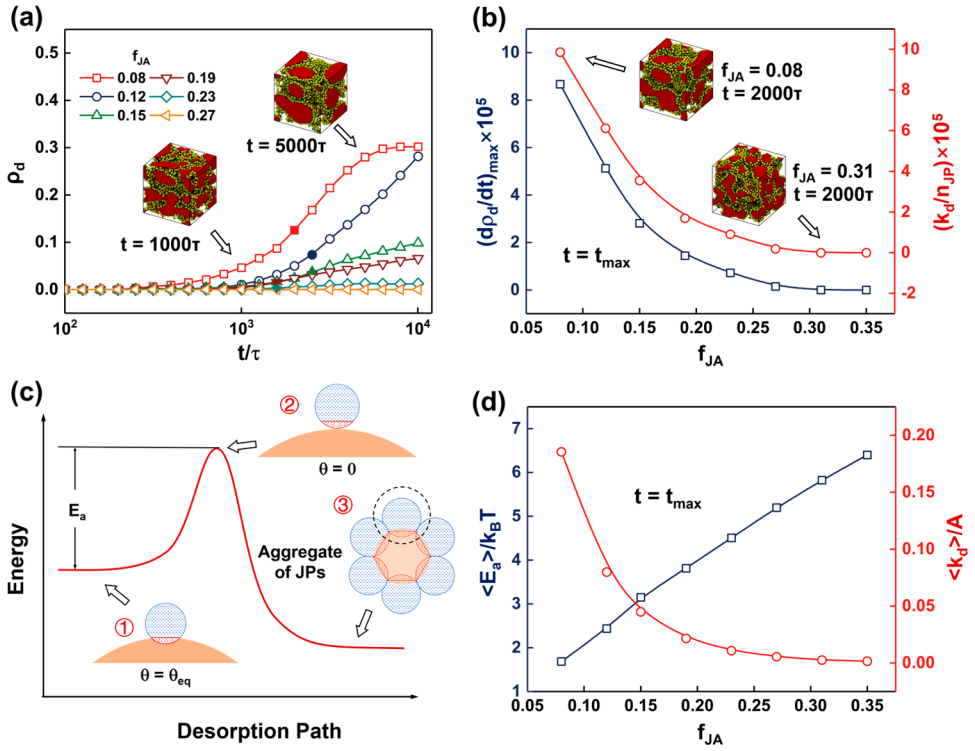

Figure 7. (a) Desorption fraction ρ_d for JPs with various f_{J_A}. Insets show the morphologies of the blend compatibilized by the JPs with f_{J_A} = 0.08 at earlier and later times. Times corresponding to maximum desorption rates $(d\rho_d/dt)_{max}$ are indicated by filled symbols. (b) Dependence of $(d\rho_d/dt)_{max}$ and the scaled desorption rate constant k_d/n_{JP} on f_{J_A}. The insets show the blend morphologies at $t = 2000\tau$ for the JPs with f_{J_A} = 0.08 and the JPs with f_{J_A} = 0.31. (c) Schematic illustration of the desorption mechanism for the JPs with f_{J_A} = 0.08. Domains rich in P_A are colored in red. Domains rich in P_B are not shown for clarity. J_A and J_B surface regions are colored in red and yellow, respectively. E_a denotes the activation energy of the desorption process. (d) Ensemble averages of the desorption activation energy E_a and the normalized desorption rate constant k_d/A (noted in eq 8) at $t = t_{max}$ for JPs with various f_{J_A}.

energetically favorable. In contrast, for the asymmetric JPs, the shape of the interfaces between the P_A and P_B networks (corresponding to $H \approx 0$) mismatches with the energetically favored shapes (corresponding to $H > 0$ or $H < 0$), which results in the breakage of the P_A (or P_B) networks at the late stage of phase separation to lower the interfacial energy of the JPs (Figure 6g). Therefore, spherical phases are formed when the asymmetric JPs are incorporated.

3.3. Compatibilization Efficiency of Asymmetric JPs.

In subsections 3.1 and 3.2, it is shown that the asymmetric JPs can act as effective morphology modifiers for polymer blends. However, they may desorb from the interfaces and form aggregates in the matrix if the fraction of the minor JP surface region is markedly low (e.g., f_{J_A} = 0.08), which indicates a reduction of the compatibilization efficiency (Figure 2d). In this subsection, the influence of the composition of the JPs on their compatibilization efficiency is characterized, and the underlying mechanism is elaborated.

Figure 7a shows the fraction ρ_d of the detached JPs (i.e., the JPs with $f_w = 0$) at various times for the blends compatibilized by the asymmetric JPs with various compositions. Only the JPs with $f_{J_A} < 0.2$ show remarkable detachment behavior, which is manifested by the notable increase in ρ_d at late times. The influence of f_{J_A} on the maximum desorption rate $(d\rho_d/dt)_{max}$ is shown in Figure 7b (note that the times t_{max} corresponding to $(d\rho_d/dt)_{max}$ are denoted by filled symbols in Figure 7a). The value of $(d\rho_d/dt)_{max}$ dramatically decreases as f_{J_A} increases from 0.05 to 0.2, suggesting that the JPs with $f_{J_A} > 0.2$ can act as efficient compatibilizers. We further analyzed the desorption rate constant k_d by the following equation

$$\frac{d\rho_d}{dt} = k_d[JP]_{inter} \tag{9}$$

where $[JP]_{inter} = n_{JP}(1 - \rho_d)$ is the molar concentration of the JPs at interfaces and n_{JP} is the number density of JPs in each box, which is a constant in the present work. Figure 7b shows the influence of f_{J_A} on the scaled desorption rate constant k_d/n_{JP} at $t = t_{max}$ for the JPs with various compositions. Similar to $(d\rho_d/dt)_{max}$, the value of k_d/n_{JP} gradually vanishes as f_{J_A} increases from ~0.2 to ~0.3, confirming the higher efficiency of the asymmetric JPs with $f_{J_A} > 0.2$. These results agree well with the morphology evolution of the blends compatibilized by the asymmetric JPs (Figure 2).

In order to explain why the efficiency of JPs rises as the f_{J_A} increases from 0.08 to 0.2, we schematically illustrate in Figure 7c the desorption path for the asymmetric JPs. Here, *position 1* corresponds to the equilibrium position of the particle. During the desorption process, the contact angle θ gradually decreases from the equilibrium angle θ_{eq} to 0 (*position 2*), and the interfacial energy $g(\theta, \varepsilon)$ increases accordingly. The difference in $g(\theta, \varepsilon)$ is treated as the activation energy E_a of the desorption process (denoted in Figure 7c). Lastly, *position 3* corresponds to the JPs in the aggregates. Because the radii of the JP aggregates are much smaller than the average size of the

https://dx.doi.org/10.1021/acs.jpcb.0c02165
J. Phys. Chem. B 2020, 124, 4619−4630

P_A domains, the interfacial energies of the JPs in the aggregates are much lower than those at the P_A/P_B interfaces, which drives the detachment of particles.

Based on the above physical picture, the values of E_a at $t = t_{max}$ were calculated for the JPs with various f_{J_A} (blue rectangles in Figure 7d). The value of E_a increases with increasing f_{J_A}, indicating stronger adsorption strengths for the JPs with larger minor surface regions. Also plotted in Figure 7d is the normalized desorption rate constant k_d/A (red circles) which is obtained by

$$k_d = A e^{-E_a/k_B T} \tag{10}$$

where A is the so-called frequency constant. It can be viewed that the shape of the k_d/A profile is quite similar to that of the k_d/n_{JP} profile (Figure 7b), which is consistent with the physical meaning of k_d noted in eq 9. These observations lead us to deduce that the efficiency of the asymmetric JPs closely depends on their compositions because the desorption activation energy is determined by the fraction of the minor JP surface regions.

3.4. Discussion. Over the past few years, Janus nanoparticles have been utilized by many researchers as high-performance compatibilizers for technologically relevant systems.[27,28,37,39,70−73] So far, most works focused on the compatibilization behavior of symmetric JPs in blending systems, while much less attention has been paid to their asymmetric counterparts. In the present work, the influence of asymmetric JPs on the morphology evolution of symmetric polymer blends during phase separation was studied. We expect that the results presented here not only shed light upon the phase separation dynamics of JP-compatibilized blends but also offer useful guidance for the design of materials with tailor-made morphologies. For example, incorporating spherical droplets of polymers with high impact or tensile strengths is a common strategy for toughening fragile plastics.[74,75] In this case, the system often shows an optimum average droplet size at which the optimized mechanical properties can be achieved.[76] In this work, we found that the asymmetric JPs have nontrivial influences on the curvature of droplets, which is inversely proportional to the droplet radius. Therefore, one may incorporate asymmetric JPs with various compositions into blending systems to tune the average size of the dispersed domains so that materials with the optimum domain size can be obtained.

As stated in the Models and Methods section, the models of JPs and homopolymers are based on the experiments of Bryson et al., who used star-like JPs containing a spherical core of cross-linked PB and two equally sized PS and PMMA hemispheres to compatibilize PS/PMMA blends. In their work, such *SBM* JPs can facilitate the blends to form bicontinuous PS and PMMA networks when the weight fractions of PS and PMMA are comparable with one another, and the JPs were exclusively located at the PS/PMMA interfaces, with the two opposite hemispheres in contact with their liked polymer phases. These observations are in good agreement with the results from our simulations, as shown in Figure 2a. However, the JPs in the experiments of Bryson et al. have symmetric structures, while the behavior of asymmetric JPs during the phase separation of polymer blends is still unclear. In comparison, the behavior of asymmetric JPs was studied in the present work, and the underlying mechanism was also elaborated, which can provide useful guidance for future experimental works concerning the morphologies of polymer blends compatibilized by asymmetric JPs.

We noticed that You et al. have also studied the influence of asymmetric JPs on the morphologies of polymer blends.[40] Specifically, they studied the morphologies after the mixing and extrusion processes for the PLA/PC blends, which can undergo a morphological transition from island structures to bicontinuous networks as the weight fraction of PC increases from 0 to 20%. They observed that the presence of asymmetric snowman-like JPs could lower the weight fraction of PC corresponding to the morphology transition, which is due to the influence of asymmetric JPs on the curvatures of PC/PLA interfaces. However, there are some remarkable differences between the work of You et al. and the present work. For example, You et al. did not consider the phase separation dynamics of the blends compatibilized by JPs, whereas our work was mainly focused on the morphology evolution during phase separation. Moreover, the systems studied by You et al. are asymmetric blends wherein the weight fraction of PC is much smaller than that of PLA, while the blends studied in this work are actually symmetric blends where the volume fractions of the two homopolymers are identical. Nevertheless, both the present work and the work of You et al. demonstrated that the asymmetric JPs could act as effective morphology modifiers for polymer blends, which is insightful for future applications.

Lastly, a comparison between the compatibilization behaviors of the JPs and the block copolymers is made. Copolymers, such as block,[42] graft,[43] random,[77] gradient,[78] and protein-like copolymers,[79] etc., are well-known compatibilizers for polymer blends, and block copolymers are the most widely adopted among them.[19,20,77] Figure S3 shows the morphology evolution of the polymer blends compatibilized by triblock copolymers (TCPs) with various compositions. It can be viewed that the composition of the TCPs hardly influences the morphology evolution of the blends; that is, P_A and P_B both form continuous networks no matter how the composition of the TCPs is varied. Specifically, Figure S3b and Figure S3d show the profiles of $\overline{V}_A(t)$ for the TCPs and JPs with various compositions, respectively. For the systems compatibilized by the asymmetric JPs with $f_{J_A} = 0.31$ and $f_{J_A} = 0.38$, the remarkable drop of the $\overline{V}_A(t)$ values at the late times indicates the morphology transition from the bicontinuous network structures to the droplets-in-matrix structures. However, such a drop is absent for the systems compatibilized by the TCPs, which confirms that the asymmetric TCPs cannot induce the morphology transitions like the JPs. Such a difference can be attributed to the fact that the TCPs lack the combination of the particulate nature with the chemical asymmetry like JPs. As a result, they cannot drive the continuous P_A networks to break into dispersed domains at the late stage of phase separation. Similar to TCPs, other compatibilizers, such as homogeneous nanoparticles and diblock copolymers, also lack the combination of the particulate nature with the chemical asymmetry of JPs. Therefore, it is expected that the mechanisms discovered in this work are unique features of the JP-compatibilized systems.

4. CONCLUSION

In the present work, phase separation dynamics of symmetric polymer blends compatibilized by Janus nanoparticles (JPs) with various compositions was studied by using DPD simulations, and the mechanism underlying the roles of

https://dx.doi.org/10.1021/acs.jpcb.0c02165
J. Phys. Chem. B 2020, 124, 4619−4630

asymmetric JPs during phase separation is elaborated for the first time. It was found that the morphology evolution of polymer blends during phase separation is significantly influenced by the composition of JPs. For the blends compatibilized by the symmetric JPs, the two polymers form bicontinuous networks, which steadily grow at the late stage of phase separation. In contrast, for those compatibilized by the asymmetric JPs, a morphology transition from bicontinuous networks to spheres-in-matrix structures occurs so that the interfacial energies of JPs can be lowered. In comparison to JPs, block copolymers lack the particulate nature of JPs and are less effective in tuning the blend morphologies. Furthermore, the activation energy of the desorption process decreases as the fraction of the minor surface region of JPs decreases. As a consequence, the JPs would desorb from the interfaces and form aggregates in the matrix if the size difference of the two JP surface regions is higher than a critical value.

■ ASSOCIATED CONTENT

Supporting Information

The Supporting Information is available free of charge at https://pubs.acs.org/doi/10.1021/acs.jpcb.0c02165.

Full details include dissipative particle dynamics, volume distribution of homopolymer domains, the influence of interaction parameters, interfacial energy of JPs, mean curvature and principal curvatures, and compatibilization behavior of triblock copolymers with various compositions (PDF)

■ AUTHOR INFORMATION

Corresponding Authors

Liquan Wang − *Shanghai Key Laboratory of Advanced Polymeric Materials, Key Laboratory for Ultrafine Materials of Ministry of Education, School of Materials Science and Engineering, East China University of Science and Technology, Shanghai 200237, China;* orcid.org/0000-0002-5141-8584; Phone: +86-21-64251615; Email: lq_wang@ecust.edu.cn

Jiaping Lin − *Shanghai Key Laboratory of Advanced Polymeric Materials, Key Laboratory for Ultrafine Materials of Ministry of Education, School of Materials Science and Engineering, East China University of Science and Technology, Shanghai 200237, China;* orcid.org/0000-0001-9633-4483; Phone: +86-21-64253370; Email: jlin@ecust.edu.cn

Authors

Qing Li − *Shanghai Key Laboratory of Advanced Polymeric Materials, Key Laboratory for Ultrafine Materials of Ministry of Education, School of Materials Science and Engineering, East China University of Science and Technology, Shanghai 200237, China*

Zhanwen Xu − *Shanghai Key Laboratory of Advanced Polymeric Materials, Key Laboratory for Ultrafine Materials of Ministry of Education, School of Materials Science and Engineering, East China University of Science and Technology, Shanghai 200237, China*

Complete contact information is available at: https://pubs.acs.org/10.1021/acs.jpcb.0c02165

Notes

The authors declare no competing financial interest.

■ ACKNOWLEDGMENTS

This work was supported by the National Natural Science Foundation of China (51621002, 51833003, 21975073, and 21774032).

■ REFERENCES

(1) Utracki, L. A. In *Polypropylene: An A-Z. reference*; Karger-Kocsis, J., Ed.; Springer: Dordrecht, The Netherlands, 1999; pp 601−605.

(2) Pernot, H.; Baumert, M.; Court, F.; Leibler, L. Design and Properties of Co-Continuous Nanostructured Polymers by Reactive Blending. *Nat. Mater.* **2002**, *1*, 54−58.

(3) McNeill, C. R. In *Semiconducting Polymer Composites*; Yang, X., Ed.; John Wiley & Sons, Inc.: Hoboken, NJ, 2013; pp 399−425.

(4) Fan, B.; Zhong, W.; Ying, L.; Zhang, D.; Li, M.; Lin, Y.; Xia, R.; Liu, F.; Yip, H.-L.; Li, N.; et al. Surpassing the 10% Efficiency Milestone for 1-cm^2 All-Polymer Solar Cells. *Nat. Commun.* **2019**, *10*, 4100−4107.

(5) Wang, S.; Min, K. Solid Polymer Electrolytes of Blends of Polyurethane and Polyether Modified Polysiloxane and Their Ionic Conductivity. *Polymer* **2010**, *51*, 2621−2628.

(6) Li, Z.; Mindemark, J.; Brandell, D.; Tominaga, Y. A Concentrated Poly(Ethylene Carbonate)/Poly(Trimethylene Carbonate) Blend Electrolyte for All-Solid-State Li Battery. *Polym. J.* **2019**, *51*, 753−760.

(7) Robeson, L. M. Polymer Blends in Membrane Transport Processes. *Ind. Eng. Chem. Res.* **2010**, *49*, 11859−11865.

(8) Haragirimana, A.; Ingabire, P. B.; Zhu, Y.; Lu, Y.; Li, N.; Hu, Z.; Chen, S. Four-Polymer Blend Proton Exchange Membranes Derived from Sulfonated Poly(Aryl Ether Sulfone)s with Various Sulfonation Degrees for Application in Fuel Cells. *J. Membr. Sci.* **2019**, *583*, 209−219.

(9) Shown, I.; Ganguly, A.; Chen, L.-C.; Chen, K.-H. Conducting Polymer-Based Flexible Supercapacitor. *Energy Sci. Eng.* **2015**, *3*, 2−26.

(10) Abeykoon, N. C.; Bonso, J. S.; Ferraris, J. P. Supercapacitor Performance of Carbon Nanofiber Electrodes Derived from Immiscible PAN/PMMA Polymer Blends. *RSC Adv.* **2015**, *5*, 19865−19873.

(11) Verkholantsev, V. V. Heterophase and Self-Stratifying Polymer Coatings. *Prog. Org. Coat.* **1995**, *26*, 31−52.

(12) Beaugendre, A.; Degoutin, S.; Bellayer, S.; Pierlot, C.; Duquesne, S.; Casetta, M.; Jimenez, M. Self-Stratifying Coatings: A Review. *Prog. Org. Coat.* **2017**, *110*, 210−241.

(13) Chalykh, A. A.; Chalykh, A. E.; Novikov, M. B.; Feldstein, M. M. Pressure-Sensitive Adhesion in the Blends of Poly(N-Vinyl Pyrrolidone) and Poly(Ethylene Glycol) of Disparate Chain Lengths. *J. Adhes.* **2002**, *78*, 667−694.

(14) Heinzmann, C.; Weder, C.; de Espinosa, L. M. Supramolecular Polymer Adhesives: Advanced Materials Inspired by Nature. *Chem. Soc. Rev.* **2016**, *45*, 342−358.

(15) de Kort, G. W.; Rastogi, S.; Wilsens, C. H. R. M. Controlling Processing, Morphology, and Mechanical Performance in Blends of Polylactide and Thermotropic Polyesters. *Macromolecules* **2019**, *52*, 6005−6017.

(16) Zhao, X.; Zhao, J.; Cao, J.-P.; Wang, X.; Chen, M.; Dang, Z.-M. Tuning the Dielectric Properties of Polystyrene/Poly(Vinylidene Fluoride) Blends by Selectively Localizing Carbon Black Nanoparticles. *J. Phys. Chem. B* **2013**, *117*, 2505−2515.

(17) Zhang, Q.; Wang, J.; Yu, J.; Guo, Z.-X. Improved Electrical Conductivity of TPU/Carbon Black Composites by Addition of COPA and Selective Localization of Carbon Black at the Interface of Sea-Island Structured Polymer Blends. *Soft Matter* **2017**, *13*, 3431−3439.

(18) Lafitte, G.; Espuche, E.; Gérard, J.-F. Polyamide 11/Poly(Hydroxy Amino Ether) Blends: Influence of the Blend Composition and Morphology on the Barrier and Mechanical Properties. *Eur. Polym. J.* **2011**, *47*, 1994−2002.

(19) Ougizawa, T.; Inoue, T. In *Polymer Blends Handbook*; Utracki, L. A., Wilkie, C. A., Eds.; Springer: Dordrecht, The Netherlands, 2014; pp 875−918.
(20) Koning, C.; van Duin, M.; Pagnoulle, C.; Jerome, R. Strategies for Compatibilization of Polymer Blends. *Prog. Polym. Sci.* **1998**, *23*, 707−757.
(21) Walther, A.; Müller, A. H. E. Janus Particles: Synthesis, Self-Assembly, Physical Properties, and Applications. *Chem. Rev.* **2013**, *113*, 5194−5261.
(22) Zhang, W.; Lin, M.; Winesett, A.; Dhez, O.; Kilcoyne, A. L.; Ade, H.; Rubinstein, M.; Shafi, K. V. P. M.; Ulman, A.; Gersappe, D.; et al. The Use of Functionalized Nanoparticles as Non-Specific Compatibilizers for Polymer Blends. *Polym. Adv. Technol.* **2011**, *22*, 65−71.
(23) Yang, Q.; Loos, K. Janus Nanoparticles inside Polymeric Materials: Interfacial Arrangement toward Functional Hybrid Materials. *Polym. Chem.* **2017**, *8*, 641−654.
(24) Honciuc, A. In *Flowing Matter*; Toschi, F., Sega, M., Eds.; Springer International Publishing: Cham, Switzerland, 2019; pp 95−136.
(25) Walther, A.; Matussek, K.; Müller, A. H. E. Engineering Nanostructured Polymer Blends with Controlled Nanoparticle Location using Janus Particles. *ACS Nano* **2008**, *2*, 1167−1178.
(26) Fernandez-Rodriguez, M. A.; Song, Y.; Rodríguez-Valverde, M. Á.; Chen, S.; Cabrerizo-Vilchez, M. A.; Hidalgo-Alvarez, R. Comparison of the Interfacial Activity between Homogeneous and Janus Gold Nanoparticles by Pendant Drop Tensiometry. *Langmuir* **2014**, *30*, 1799−1804.
(27) Bahrami, R.; Löbling, T. I.; Gröschel, A. H.; Schmalz, H.; Müller, A. H. E.; Altstädt, V. The Impact of Janus Nanoparticles on the Compatibilization of Immiscible Polymer Blends under Technologically Relevant Conditions. *ACS Nano* **2014**, *8*, 10048−10056.
(28) Wang, H.; Fu, Z.; Zhao, X.; Li, Y.; Li, J. Reactive Nanoparticles Compatibilized Immiscible Polymer Blends: Synthesis of Reactive SiO_2 with Long Poly(Methyl Methacrylate) Chains and the In Situ Formation of Janus SiO_2 Nanoparticles Anchored Exclusively at the Interface. *ACS Appl. Mater. Interfaces* **2017**, *9*, 14358−14370.
(29) Pang, X.; Wan, C.; Wang, M.; Lin, Z. Strictly Biphasic Soft and Hard Janus Structures: Synthesis, Properties, and Applications. *Angew. Chem., Int. Ed.* **2014**, *53*, 5524−5538.
(30) Gröschel, A. H.; Walther, A.; Löbling, T. I.; Schmelz, J.; Hanisch, A.; Schmalz, H.; Müller, A. H. E. Facile, Solution-Based Synthesis of Soft, Nanoscale Janus Particles with Tunable Janus Balance. *J. Am. Chem. Soc.* **2012**, *134*, 13850−13860.
(31) Percebom, A. M.; Giner-Casares, J. J.; Claes, N.; Bals, S.; Loh, W.; Liz-Marzán, L. M. Janus Gold Nanoparticles Obtained via Spontaneous Binary Polymer Shell Segregation. *Chem. Commun.* **2016**, *52*, 4278−4281.
(32) Nisisako, T. Recent Advances in Microfluidic Production of Janus Droplets and Particles. *Curr. Opin. Colloid Interface Sci.* **2016**, *25*, 1−12.
(33) Wang, B.; Li, B.; Zhao, B.; Li, C. Y. Amphiphilic Janus Gold Nanoparticles via Combining "Solid-State Grafting-to" and "Grafting-from" Methods. *J. Am. Chem. Soc.* **2008**, *130*, 11594−11595.
(34) Wang, F.; Pauletti, G. M.; Wang, J.; Zhang, J.; Ewing, R. C.; Wang, Y.; Shi, D. Dual Surface-Functionalized Janus Nanocomposites of Polystyrene/Fe_3O_4@SiO_2 for Simultaneous Tumor Cell Targeting and Stimulus-Induced Drug Release. *Adv. Mater.* **2013**, *25*, 3485−3489.
(35) Li, X.; Zhou, L.; Wei, Y.; El-Toni, A. M.; Zhang, F.; Zhao, D. Anisotropic Growth-Induced Synthesis of Dual-Compartment Janus Mesoporous Silica Nanoparticles for Bimodal Triggered Drugs Delivery. *J. Am. Chem. Soc.* **2014**, *136*, 15086−15092.
(36) Zhang, L.; Chen, Y.; Li, Z.; Li, L.; Saint-Cricq, P.; Li, C.; Lin, J.; Wang, C.; Su, Z.; Zink, J. I. Tailored Synthesis of Octopus-Type Janus Nanoparticles for Synergistic Actively-Targeted and Chemo-Photothermal Therapy. *Angew. Chem., Int. Ed.* **2016**, *55*, 2118−2121.
(37) Xu, W.; Chen, J.; Chen, S.; Chen, Q.; Lin, J.; Liu, H. Study on the Compatibilizing Effect of Janus Particles on Liquid Isoprene Rubber/Epoxy Resin Composite Materials. *Ind. Eng. Chem. Res.* **2017**, *56*, 14060−14068.
(38) Cheng, W.; Xu, Z.; Chen, S.; Ai, J.; Lin, J.; Lin, J.; Chen, Q. Compatibilization Behavior of Double Spherical TETA-SiO_2@PDVB Janus Particles Anchored at the Phase Interface of Acrylic Resin/Epoxy Resin (AR/EP) Polymer Blends. *ACS Omega* **2019**, *4*, 17607−17614.
(39) Parpaite, T.; Otazaghine, B.; Caro, A. S.; Taguet, A.; Sonnier, R.; Lopez-Cuesta, J. M. Janus Hybrid Silica/Polymer Nanoparticles as Effective Compatibilizing Agents for Polystyrene/Polyamide-6 Melted Blends. *Polymer* **2016**, *90*, 34−44.
(40) You, W.; Yu, W. Onset Reduction and Stabilization of Cocontinuous Morphology in Immiscible Polymer Blends by Snowmanlike Janus Nanoparticles. *Langmuir* **2018**, *34*, 11092−11100.
(41) Lyu, S.; Jones, T. D.; Bates, F. S.; Macosko, C. W. Role of Block Copolymers on Suppression of Droplet Coalescence. *Macromolecules* **2002**, *35*, 7845−7855.
(42) Pu, G.; Luo, Y.; Wang, A.; Li, B. Tuning Polymer Blends to Cocontinuous Morphology by Asymmetric Diblock Copolymers as the Surfactants. *Macromolecules* **2011**, *44*, 2934−2943.
(43) Shao, Y.; Yang, Z.; Deng, B.; Yin, B.; Yang, M. Tuning PVDF/PS/HDPE Polymer Blends to Tri-Continuous Morphology by Grafted Copolymers as the Compatibilizers. *Polymer* **2018**, *140*, 188−197.
(44) Li, F.; Zhao, X.; Wang, H.; Chen, Q.; Wang, S.; Chen, Z.; Zhou, X.; Fan, W.; Li, Y.; You, J. Sub-100 nm Cocontinuous Structures Fabricated in Immiscible Commodity Polymer Blend with Extremely Low Volume/Viscosity Ratio. *ACS Appl. Polym. Mater.* **2019**, *1*, 124−129.
(45) Xu, Z.; Lin, J.; Zhang, Q.; Wang, L.; Tian, X. Theoretical Simulations of Nanostructures Self-Assembled from Copolymer Systems. *Polym. Chem.* **2016**, *7*, 3783−3811.
(46) Zhang, Q.; Lin, J.; Wang, L.; Xu, Z. Theoretical Modeling and Simulations of Self-Assembly of Copolymers in Solution. *Prog. Polym. Sci.* **2017**, *75*, 1−30.
(47) Wei, D.; Li, Y.; Liao, Q.; Jin, X. Molecular Dynamics Simulation on Phase Separation of Polymer Blend Systems. *Chem. J. Chin. Univ.* **2006**, *27*, 156−160.
(48) Kim, S. H.; Jo, W. H.; Kim, J. Monte Carlo Simulation of Phase Separation Dynamics of A Polymer Blend in the Presence of Block Copolymer. 2. Effect of Block Copolymer Composition. *Macromolecules* **1996**, *29*, 6933−6940.
(49) Müller, M.; Smith, G. D. Phase Separation in Binary Mixtures Containing Polymers: A Quantitative Comparison of Single-Chain-in-Mean-Field Simulations and Computer Simulations of the Corresponding Multichain Systems. *J. Polym. Sci., Part B: Polym. Phys.* **2005**, *43*, 934−958.
(50) Shimizu, R.; Tanaka, H. A Novel Coarsening Mechanism of Droplets in Immiscible Fluid Mixtures. *Nat. Commun.* **2015**, *6*, 7407−7417.
(51) Groot, R. D.; Warren, P. B. Dissipative Particle Dynamics: Bridging the Gap between Atomistic and Mesoscopic Simulation. *J. Chem. Phys.* **1997**, *107*, 4423−4435.
(52) Huang, M.; Li, Z.; Guo, H. The Effect of Janus Nanospheres on the Phase Separation of Immiscible Polymer Blends via Dissipative Particle Dynamics Simulations. *Soft Matter* **2012**, *8*, 6834−6845.
(53) Zhou, Y.; Huang, M.; Lu, T.; Guo, H. Nanorods with Different Surface Properties in Directing the Compatibilization Behavior and the Morphological Transition of Immiscible Polymer Blends in Both Shear and Shear-Free Conditions. *Macromolecules* **2018**, *51*, 3135−3148.
(54) Chen, S.; Yong, X. Janus Nanoparticles Enable Entropy-Driven Mixing of Bicomponent Hydrogels. *Langmuir* **2019**, *35*, 14840−14848.
(55) Li, Q.; Wang, L.; Lin, J.; Zhang, L. Distinctive Phase Separation Dynamics of Polymer Blends: Roles of Janus Nanoparticles. *Phys. Chem. Chem. Phys.* **2019**, *21*, 2651−2658.

https://dx.doi.org/10.1021/acs.jpcb.0c02165
J. Phys. Chem. B 2020, 124, 4619−4630

(56) Hore, M. J. A.; Laradji, M. Microphase Separation Induced by Interfacial Segregation of Isotropic, Spherical Nanoparticles. *J. Chem. Phys.* **2007**, *126*, 244903−244911.
(57) Yang, Y.; Chen, P.; Cao, Y.; Huang, Z.; Zhu, G.; Xu, Z.; Dai, X.; Chen, S.; Miao, B.; Yan, L.-T. How Implementation of Entropy in Driving Structural Ordering of Nanoparticles Relates to Assembly Kinetics: Insight into Reaction-Induced Interfacial Assembly of Janus Nanoparticles. *Langmuir* **2018**, *34*, 9477−9488.
(58) Xu, Z.; Lin, J.; Zhang, L.; Tian, X.; Wang, L. Modulation of Molecular Orientation Enabling High Photovoltaic Performance of Block Copolymer Nanostructures. *Mater. Chem. Front.* **2019**, *3*, 2627−2636.
(59) Bryson, K. C.; Löbling, T. I.; Müller, A. H. E.; Russell, T. P.; Hayward, R. C. Using Janus Nanoparticles to Trap Polymer Blend Morphologies during Solvent-Evaporation-Induced Demixing. *Macromolecules* **2015**, *48*, 4220−4227.
(60) Langer, J. S. Theory of Spinodal Decomposition in Alloys. *Ann. Phys.* **1971**, *65*, 53−86.
(61) Snyder, H. L.; Meakin, P. Details of Phase Separation Processes in Polymer Blends. *J. Polym. Sci., Polym. Symp.* **1985**, *73*, 217−239.
(62) HOOMD-blue. http://glotzerlab.engin.umich.edu/hoomd-blue/ (accessed May 8, 2020).
(63) Phillips, C. L.; Anderson, J. A.; Glotzer, S. C. Pseudo-Random Number Generation for Brownian Dynamics and Dissipative Particle Dynamics Simulations on GPU Devices. *J. Comput. Phys.* **2011**, *230*, 7191−7201.
(64) Glaser, J.; Nguyen, T. D.; Anderson, J. A.; Lui, P.; Spiga, F.; Millan, J. A.; Morse, D. C.; Glotzer, S. C. Strong Scaling of General-Purpose Molecular Dynamics Simulations on GPUs. *Comput. Phys. Commun.* **2015**, *192*, 97−107.
(65) Yan, L.-T.; Popp, N.; Ghosh, S.-K.; Böker, A. Self-Assembly of Janus Nanoparticles in Diblock Copolymers. *ACS Nano* **2010**, *4*, 913−920.
(66) Rapaport, D. C. *The Art of Molecular Dynamics Simulation*, 2nd ed.; Cambridge University Press: Cambridge, U.K., 2004; pp 44−82.
(67) Holloway, J. L.; Lowman, A. M.; Palmese, G. R. The Role of Crystallization and Phase Separation in the Formation of Physically Cross-Linked PVA Hydrogels. *Soft Matter* **2013**, *9*, 826−833.
(68) Zhang, X.; Li, W.; Song, P.; You, B.; Sun, G. Double-Cross-Linking Strategy for Preparing Flexible, Robust, and Multifunctional Polyimide Aerogel. *Chem. Eng. J.* **2020**, *381*, 122784−122794.
(69) Hirose, Y.; Komura, S.; Nonomura, Y. Adsorption of Janus Particles to Curved Interfaces. *J. Chem. Phys.* **2007**, *127*, 054707−054712.
(70) Nie, H.; Liang, X.; He, A. Enthalpy-Enhanced Janus Nanosheets for Trapping Nonequilibrium Morphology of Immiscible Polymer Blends. *Macromolecules* **2018**, *51*, 2615−2620.
(71) Bahrami, R.; Löbling, T. I.; Schmalz, H.; Müller, A. H. E.; Altstädt, V. Synergistic Effects of Janus Particles and Triblock Terpolymers on Toughness of Immiscible Polymer Blends. *Polymer* **2017**, *109*, 229−237.
(72) Wang, H.; Dong, W.; Li, Y. Compatibilization of Immiscible Polymer Blends Using In Situ Formed Janus Nanomicelles by Reactive Blending. *ACS Macro Lett.* **2015**, *4*, 1398−1403.
(73) Han, B.; Xia, W.; Liu, K.; Tian, F.; Chen, Y.; Wang, X.; Liang, F.; Yang, Z. Janus Nanoparticles for Improved Dentin Bonding. *ACS Appl. Mater. Interfaces* **2018**, *10*, 8519−8526.
(74) Bärwinkel, S.; Seidel, A.; Hobeika, S.; Hufen, R.; Mörl, M.; Altstädt, V. Morphology Formation in PC/ABS Blends During Thermal Processing and the Effect of the Viscosity Ratio of Blend Partners. *Materials* **2016**, *9*, 659−677.
(75) Wu, F.; Misra, M.; Mohanty, A. K. Tailoring the Toughness of Sustainable Polymer Blends from Biodegradable Plastics via Morphology Transition Observed by Atomic Force Microscopy. *Polym. Degrad. Stab.* **2020**, *173*, 109066−109076.
(76) Podshivalov, A.; Besson, F.; Budtova, T.; Bronnikov, S. Morphology and Improved Impact Strength of Cellulose Acetate Butyrate Blended with Polyethylene Copolymer. *eXPRESS Polym. Lett.* **2018**, *12*, 856−866.
(77) Xie, X.-M.; Sui, X. In *Compatibilization of Polymer Blends*; Ajitha, A. R., Thomas, S., Eds.; Elsevier: 2020; pp 145−177.
(78) Kim, J.; Gray, M. K.; Zhou, H.; Nguyen, S. T.; Torkelson, J. M. Polymer Blend Compatibilization by Gradient Copolymer Addition during Melt Processing: Stabilization of Dispersed Phase to Static Coarsening. *Macromolecules* **2005**, *38*, 1037−1040.
(79) Malik, R.; Hall, C. K.; Genzer, J. Effect of Protein-Like Copolymers Composition on the Phase Separation Dynamics of a Polymer Blend: A Monte Carlo Simulation. *Macromolecules* **2013**, *46*, 4207−4214.

https://dx.doi.org/10.1021/acs.jpcb.0c02165
J. Phys. Chem. B 2020, 124, 4619−4630